

# A general guide to design of falling film evaporators utilized in multi-effect desalination units operating at high vapor qualities under a sub-atmospheric condition

S. Bigham <sup>a,\*</sup>, R. KouhiKamali <sup>b</sup>, M. P. Zadeh <sup>c</sup>

<sup>a</sup> Department of Mechanical and Aerospace Engineering, University of Florida, Gainesville, FL 32611, United States

<sup>b</sup> Department of Mechanical Engineering, University of Guilan, Guilan, Iran

<sup>c</sup> Mechanical & Industrial Engineering Department, Louisiana State University, Baton Rouge, LA 70803, United States



## ARTICLE INFO

### Article history:

Received 15 July 2014

Received in revised form

14 February 2015

Accepted 27 February 2015

Available online 23 March 2015

### Keywords:

Falling film evaporation

MED (multi effect desalination) units

VOF (volume of fluid) method

Performance curve

Two-phase flows

## ABSTRACT

Existing heat transfer correlations poorly predict the thermal performance of falling film evaporators utilized in MED (multi effect desalination) units. At typical operating conditions of these units, most correlations suggest that the two-phase heat transfer coefficient increases with the mass flow rate and is independent of the wall superheat. Although these correlations are valid within their particular range of parameters, they are not suitable prediction tools for MED units as they operate at high vapor qualities under a sub-atmospheric condition. In addition, strong interconnected effects of the wall superheat and the mass flow rate on the thermal performance are often unavoidable in the MED units. The present study aims to elucidate the thermal transport processes of the falling film evaporators utilized in these MED units. Results show, at a constant value of  $\Delta T/m_f$  which is a design characteristic of these units, the average heat transfer coefficient first decreases and then increases as the inlet mass flow rate increases. Result also indicate the wall superheat for this transition increases at higher values of  $\Delta T/m_f$ . The detailed thermo-hydrodynamic physics of the involved transport processes is elucidated using the VOF (volume of fluid) multiphase model in the curvilinear coordinate.

© 2015 Elsevier Ltd. All rights reserved.

## 1. Introduction

Evaporation of falling two-phase flows over a tube bundle, falling film evaporation, is an important problem taking place in many industrial devices such as evaporators, condensers and sea water desalination units [1,2]. Falling film evaporation is also a common phenomenon in the petrochemical industries as well as large heat pump systems [3].

Heat transfer coefficient is the most important parameter in the design stage of many thermal devices utilizing an evaporating falling film over a tube bundle. Although falling film evaporation over a tube bundle has a wide range of applications, most available heat transfer correlations are valid for their particular range of parameters [1–7]. Most correlations restrict their range of validity to low vapor qualities or atmospheric conditions. As a result, they cannot precisely predict the thermal performance of the MED

(multi effect desalination) units operating at high vapor qualities under a vacuum condition. Therefore, new studies focusing on the thermo-hydrodynamic flow conditions of these thermal devices are necessary to further advance the design stage, operation phase and future optimization of such units.

A state-of-the-art review of falling film evaporation on single tubes and tube bundles is presented by Thome [1]. Both plain and enhanced tubes are addressed in his survey. He concluded that the enhanced tubes provide a very high level of heat transfer augmentation for falling film evaporation on horizontal bundles, sharply reducing the required refrigerant charge compared to flooded evaporator designs. Chyu and Bergles [8] developed an analytical model to predict the heat transfer coefficient of falling-film evaporation on a horizontal tube. Their solution is consisted of four separate zones around the circumference of the tube: stagnation flow, impingement, thermal developing/developed with heating of the liquid, and fully developed region with surface evaporation. Their results showed that for the case of saturated falling films, convective heat transfer leads to evaporation at the liquid–vapor interface. By increasing heat flux, nucleate boiling

\* Corresponding author.

E-mail address: [bighams@ufl.edu](mailto:bighams@ufl.edu) (S. Bigham).

<b>Nomenclature</b>	
$k$	turbulent kinetic energy
$h$	heat transfer coefficient ( $\text{W}/\text{m}^2\text{-K}$ )
$p$	pressure
$J$	Jacobian of the coordinate transformation
$k$	turbulent kinetic energy, $\text{m}^2/\text{s}^2$
$u$	velocity component in $x$ -direction ( $\text{m}/\text{s}$ )
$v$	velocity component in $y$ -direction ( $\text{m}/\text{s}$ )
$U$	velocity component in $\xi$ -direction ( $\text{m}/\text{s}$ )
$V$	velocity component in $\eta$ -direction ( $\text{m}/\text{s}$ )
$C_v$	specific heat capacity ( $\text{J}/\text{kg}\text{-K}$ )
$D_{Sm}$	mean Sauter diameter ( $\text{m}$ )
$K$	thermal conductivity ( $\text{W}/\text{m}\text{-K}$ )
$E$	enthalpy ( $\text{J}/\text{kg}$ )
$g_{11}$	grid parameter
$g_{12}$	grid parameter
$g_{22}$	grid parameter
$n$	normal vector
$\dot{m}_f$	inlet mass flow rate of the feed water
$x$	horizontal coordinate
$y$	vertical coordinate
$S$	source term
$h_{lv}$	latent heat ( $\text{J}/\text{kg}$ )
<i>Greek symbols</i>	
$\alpha$	volume fraction
$\beta$	mass transfer-time relaxation parameter
$\rho$	density ( $\text{kg}/\text{m}^3$ )
$\sigma$	surface tension
$\mu$	dynamic viscosity ( $\text{Pa}\cdot\text{s}$ )
$\kappa$	surface curvature
$\xi$	curvilinear horizontal coordinate
$\eta$	curvilinear vertical coordinate
$\epsilon$	the turbulent dissipation rate
$\chi$	average specific heat capacity ( $\text{J}/\text{kg}\text{-K}$ )
$\theta$	contact angle
<i>Subscripts</i>	
l	liquid water
sat	saturation condition
v	vapor
f	feed water
<i>Superscripts</i>	
C	contravariant velocities

occurs; vapor bubbles grow and are carried along by the film flow such that both thin falling-film evaporation and nucleate boiling play a role in the heat transfer process, depending mainly on the heat flux and liquid mass flow. Falling thin-film heat transfer on horizontal smooth tubes had been examined by Parken et al. [9]. They found that the average boiling heat transfer coefficients enhance by an increase in the feed water temperature, tube-wall heat flux, and flow rate. Yang and Shen [10] carried out an experimental study on falling film heat transfer outside horizontal tubes in order to investigate the effects of different parameters on heat transfer coefficient. Their results showed that the heat transfer coefficient of falling film evaporation increases by an increase in the liquid feed rate, evaporation boiling temperature and heat flux. Habert and Thome [11,12] performed falling-film evaporation measurements on a single tube row bundle and a three-row tube bundle to obtain local heat transfer coefficients. They observed that in a single-row configuration, the heat transfer coefficient is mostly constant for a given heat flux in the plateau region until the onset of dry-out is reached, followed by increasing dry-out of the surface with a rapid decrease of the heat transfer toward the vapor-phase heat transfer value at complete dry-out. They also concluded that the bundle effects were detrimental to thermal performance.

With the recent advent of high-speed computers, the numerical techniques for the simulation of two-phase flow with liquid–vapor phase change have become very promising. Yang et al. [13] performed VOF simulations of boiling flow of R141B in a horizontal coiled tube. The calculations treated the phase change as a local temperature dictated process based on a quasi thermo-equilibrium assumption, which yielded a flow pattern in a good agreement with the experimental observation. Son and Dhir [14] used a coordinate transformation technique supplemented by a numerical grid generation method to simulate film boiling for both two-dimensional and axisymmetric flows. Yuan et al. [15] presented a numerical method for the simulation of boiling flows on non-orthogonal body-fitted coordinates via VOF (volume of fluid) method based on PLIC (piecewise linear interface construction) for tracking liquid–vapor interface. They simulated natural convection film boiling and forced convection film boiling on a sphere at saturated conditions. In this work, boundary

conditions have curvy walls. Considerable efforts have been devoted to simulate fluid flow and heat transfer in curved geometries [16–20]. In these simulations, a transformation from the physical space to the computational domain is performed. This transformation is accomplished by specifying a generalized coordinate system mapping the nonrectangular grid system of the physical space to a rectangular uniform grid spacing in the computational space [16,17,20].

The present study aims to understand the interconnected effects of the wall superheat and the inlet mass flow rate on the thermal performance of MED units operating at high vapor qualities under a sub-atmospheric condition. Practical thermal performance curves of falling film evaporators utilized in the MED units will be presented. The performance curves provide basic guidelines for the design stage as well as the operation phase of the MED units. Finally, the obtained performance curves will be compared with two experimental MED units.

## 2. Mathematical formulation

The tube bundle layout employed for the current study is schematically shown in Fig. 1. In the falling film process, the liquid flowing downward by gravity will create a liquid layer film over the tube walls. As the liquid film flows around the tubes, the liquid temperatures increases to the saturation temperature in which the evaporation process starts occurring. The volume fraction of liquid and vapor phases is obtained by solving the continuity equation for each individual phase. Since the volume fractions of two phases sum to unity in each computational cell, the liquid volume fraction can be calculated as follows:

$$\alpha_l = 1 - \alpha_v \quad (1)$$

In the VOF (Volume of Fluid) method, it is assumed that all phases have a shared velocity field determined from RANS (Reynolds-averaged Navier–Stokes) equations. Once the velocity field is obtained, the continuity equation can be solved. For the vapor phase, this equation has the following form:

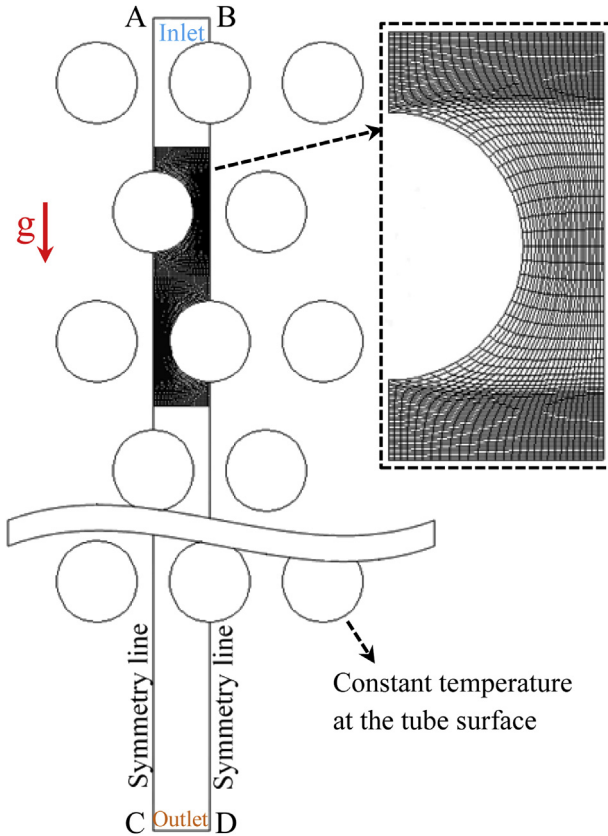


**Fig. 1.** The physical domain of the tube bundle.

$$\frac{\partial}{\partial t}(\rho_l \alpha_l) + \frac{\partial}{\partial x}(\rho_l \alpha_l u) + \frac{\partial}{\partial y}(\rho_l \alpha_l v) = S_l \quad (2)$$

Since the physical domain of the present study has curved surfaces, this equation needs to be transferred to a general non-orthogonal curvilinear coordinate framework with  $(\xi, \eta)$  as independent variables [21,22]. In the curvilinear coordinate, the continuity equation has the following form [16,21–25]:

$$J \frac{\partial}{\partial t}(\rho_l \alpha_l) + \frac{\partial}{\partial \xi}(\rho_l \alpha_l U^C) + \frac{\partial}{\partial \eta}(\rho_l \alpha_l V^C) = JS_l \quad (3)$$

where

$$U^C = (uy_\eta - vx_\eta), \quad V^C = (-uy_\xi + vx_\xi), \quad J = (x_\xi y_\eta - x_\eta y_\xi)$$

Using the above equations, the volume fraction of each phase is determined. It should be noted, however, the phase volume fraction values do not uniquely identify the interface between the phases. Several specialized techniques are developed to track the interfacial geometry accurately [23]. The VOF method assumes that the interface is a continuous and piecewise smooth line in each computational cell. In fact, these piecewise linear segments construct the interface. The slope of interface line is determined from the interface norm. These lines divide the computational cell into sections in such a way that the volume of the phases in the cell correspond with the values of the phase volume fractions in that cell. The problem of finding these piecewise smooth lines is really challenging and several techniques are developed. These techniques are generally known as the PLIC (Piecewise Linear Interface Calculation) algorithms [24].

As mentioned before, there is a unique velocity field shared by all phases in VOF method. This velocity field is obtained by solving the momentum equations throughout the domain. Falling film evaporation is inherently turbulent. Therefore, the RANS (Reynolds-averaged Navier–Stokes) equations which are time-averaged equations of motion for fluid flow are utilized [25]. **Table 1** summarizes the RANS equations in the curvilinear coordinate.

The velocity field is subject to the incompressibility constraint:

$$\frac{\partial}{\partial \xi}(U^C) + \frac{\partial}{\partial \eta}(V^C) = 0 \quad (4)$$

In order to avoid abrupt changes across very thin interfaces, a volume weighted interpolation scheme is used for mixture properties in the RANS equations as below:

$$\rho = \alpha_l \rho_l + \alpha_v \rho_v \quad (5)$$

$$\mu = \alpha_l \mu_l + \alpha_v \mu_v \quad (6)$$

In the RANS equations,  $n$ ,  $\sigma$  and  $\kappa$  are surface normal vector, surface tension and surface curvature respectively. There are several ways to determine the normal vector [26]. Here, the gradient of volume of fraction is used to calculate the normal vector as [27,28]:

$$\vec{n} = \vec{\nabla} \alpha_l \quad (7)$$

A typical computational cell and the normal vector to the segment are schematically shown in Fig. 2.a. The normal vector can be estimated in this cell as follows [28]:

$$n_\xi = \frac{1}{\Delta \xi} \left( \alpha_{i+1,j+1}^l + 2\alpha_{i+1,j}^l + \alpha_{i+1,j-1}^l - \alpha_{i-1,j+1}^l - 2\alpha_{i-1,j}^l \right. \\ \left. - \alpha_{i-1,j-1}^l \right) \quad (8)$$

$$n_\eta = \frac{1}{\Delta \eta} \left( \alpha_{i+1,j+1}^l + 2\alpha_{i,j+1}^l + \alpha_{i-1,j+1}^l - \alpha_{i+1,j-1}^l - 2\alpha_{i,j-1}^l \right. \\ \left. - \alpha_{i-1,j-1}^l \right) \quad (9)$$

**Fig. 2.b** depicts fluid interface near rigid boundaries. For a boundary cell, the surface normal vector can be directly determined based on the static contact angle,  $\theta_{eq}$ .

$$\vec{n} = (\cos \theta_{eq}) \vec{\xi} + (\sin \theta_{eq}) \vec{\eta} \quad (10)$$

The curvature,  $\kappa$ , can be calculated as [28]:

$$\kappa = \frac{1}{|\vec{n}|} \left[ \left( \frac{\vec{n}}{|\vec{n}|} \cdot \vec{\nabla} \right) |\vec{n}| - (\vec{\nabla} \cdot \vec{n}) \right] \quad (11)$$

In the VOF model, a unique energy equation is solved throughout the computational domain and the obtained temperature is shared by all phases.

$$J \frac{\partial}{\partial t}(\rho \chi T) + \frac{\partial}{\partial \xi}(\rho \chi U^C T) + \frac{\partial}{\partial \eta}(\rho \chi V^C T) \\ = \frac{\partial}{\partial \xi} \left( q_{11} \frac{\partial}{\partial \xi} (KT) \right) + \frac{\partial}{\partial \xi} \left( q_{12} \frac{\partial}{\partial \eta} (KT) \right) + \frac{\partial}{\partial \eta} \left( q_{12} \frac{\partial}{\partial \xi} (KT) \right) \\ + \frac{\partial}{\partial \eta} \left( q_{22} \frac{\partial}{\partial \eta} (KT) \right) + JS_E \quad (12)$$

where the thermal conductivity is calculated as:

**Table 1**

The momentum equations in the curvilinear coordinate [16,21–25].

RANS equation in  $\xi$ -direction:

$$\int \frac{\partial}{\partial t} (\rho u) + \frac{\partial}{\partial \xi} (\rho u U^C) + \frac{\partial}{\partial \eta} (\rho u V^C) = \left\{ \frac{\partial}{\partial \xi} \left( g_{11} \mu \frac{\partial u}{\partial \xi} \right) + \frac{\partial}{\partial \xi} \left( g_{12} \mu \frac{\partial u}{\partial \eta} \right) + \frac{\partial}{\partial \eta} \left( g_{22} \mu \frac{\partial u}{\partial \xi} \right) \right\} - \left\{ \frac{\partial}{\partial \xi} (y_\eta p) - \frac{\partial}{\partial \eta} (y_\xi p) \right\} + \left( \frac{2\rho\sigma\kappa}{\rho_l + \rho_v} \right) (y_\eta n_\xi - y_\xi n_\eta) + JS_{uvd} + JS_{uturb}$$

RANS equation in  $\eta$ -direction:

$$\int \frac{\partial}{\partial t} (\rho v) + \frac{\partial}{\partial \xi} (\rho v U^C) + \frac{\partial}{\partial \eta} (\rho v V^C) = \left\{ \frac{\partial}{\partial \xi} \left( g_{11} \mu \frac{\partial v}{\partial \xi} \right) + \frac{\partial}{\partial \xi} \left( g_{12} \mu \frac{\partial v}{\partial \eta} \right) + \frac{\partial}{\partial \eta} \left( g_{22} \mu \frac{\partial v}{\partial \xi} \right) \right\} - \left\{ \frac{\partial}{\partial \xi} (x_\eta p) + \frac{\partial}{\partial \eta} (x_\xi p) \right\} - \rho Jg \\ + \left( \frac{2\rho\sigma\kappa}{\rho_l + \rho_v} \right) (-x_\eta n_\xi + x_\xi n_\eta) + JS_{vvd} + JS_{vturb}$$

Turbulent kinetic energy  $k$ :

$$\int \frac{\partial}{\partial t} (\rho k) + \frac{\partial}{\partial \xi} (\rho k U^C) + \frac{\partial}{\partial \eta} (\rho k V^C) = \left\{ \frac{\partial}{\partial \xi} \left( g_{11} (\mu + \mu_t) \frac{\partial k}{\partial \xi} \right) + \frac{\partial}{\partial \xi} \left( g_{12} (\mu + \mu_t) \frac{\partial k}{\partial \eta} \right) + \frac{\partial}{\partial \eta} \left( g_{22} (\mu + \mu_t) \frac{\partial k}{\partial \eta} \right) \right\} - \rho \epsilon + JG_k$$

The turbulent dissipation rate  $\epsilon$ :

$$\frac{\partial}{\partial t} (\rho \epsilon) + \frac{\partial}{\partial \xi} (\rho \epsilon U^C) + \frac{\partial}{\partial \eta} (\rho \epsilon V^C) = \left\{ \frac{\partial}{\partial \xi} \left( g_{11} (\mu + 0.77 \mu_t) \frac{\partial \epsilon}{\partial \xi} \right) + \frac{\partial}{\partial \xi} \left( g_{12} (\mu + 0.77 \mu_t) \frac{\partial \epsilon}{\partial \eta} \right) + \frac{\partial}{\partial \eta} \left( g_{22} (\mu + 0.77 \mu_t) \frac{\partial \epsilon}{\partial \eta} \right) \right\} - 1.92 \rho \frac{k^2}{k} + \frac{1.44 \epsilon}{k} JG_k$$

where

$$JS_{uvd} = \frac{1}{3} \frac{\partial}{\partial \xi} \left[ \frac{1}{J} \left( y_\eta^2 \mu \frac{\partial u}{\partial \xi} - y_\xi y_\eta \mu \frac{\partial u}{\partial \eta} - x_\eta y_\eta \mu \frac{\partial v}{\partial \xi} + x_\xi y_\eta \mu \frac{\partial v}{\partial \eta} \right) \right] + \frac{1}{3} \frac{\partial}{\partial \eta} \left[ \frac{1}{J} \left( -y_\xi y_\eta \mu \frac{\partial u}{\partial \xi} + y_\xi^2 \mu \frac{\partial u}{\partial \eta} + x_\eta y_\xi \mu \frac{\partial v}{\partial \xi} - x_\xi y_\xi \mu \frac{\partial v}{\partial \eta} \right) \right] \\ JS_{uturb} = \sum_{j=1}^2 \frac{\partial}{\partial x_j} (-\rho u' u'_j) = \left\{ \frac{\partial}{\partial \xi} \left( g_{11} \mu_t \frac{\partial u}{\partial \xi} \right) + \frac{\partial}{\partial \xi} \left( g_{12} \mu_t \frac{\partial u}{\partial \eta} \right) + \frac{\partial}{\partial \eta} \left( g_{12} \mu_t \frac{\partial u}{\partial \xi} \right) + \frac{\partial}{\partial \eta} \left( g_{22} \mu_t \frac{\partial u}{\partial \eta} \right) \right\} + \frac{1}{3} \frac{\partial}{\partial \xi} \left[ \frac{1}{J} \left( y_\eta^2 \mu_t \frac{\partial u}{\partial \xi} - y_\xi y_\eta \mu_t \frac{\partial u}{\partial \eta} - x_\eta y_\eta \mu_t \frac{\partial v}{\partial \xi} + x_\xi y_\eta \mu_t \frac{\partial v}{\partial \eta} \right) \right] \\ + \frac{1}{3} \frac{\partial}{\partial \eta} \left[ \frac{1}{J} \left( -y_\xi y_\eta \mu_t \frac{\partial u}{\partial \xi} + y_\xi^2 \mu_t \frac{\partial u}{\partial \eta} + x_\eta y_\xi \mu_t \frac{\partial v}{\partial \xi} - x_\xi y_\xi \mu_t \frac{\partial v}{\partial \eta} \right) \right] - \frac{2}{3} \rho \left\{ \frac{\partial}{\partial \xi} (y_\eta k) - \frac{\partial}{\partial \eta} (y_\xi k) \right\} \\ JS_{vvd} = \frac{1}{3} \frac{\partial}{\partial \xi} \left[ \frac{1}{J} \left( -x_\eta y_\eta \mu \frac{\partial u}{\partial \xi} + x_\eta y_\xi \mu \frac{\partial u}{\partial \eta} + x_\eta^2 \mu \frac{\partial v}{\partial \xi} - x_\xi x_\eta \mu \frac{\partial v}{\partial \eta} \right) \right] + \frac{1}{3} \frac{\partial}{\partial \eta} \left[ \frac{1}{J} \left( -x_\xi y_\eta \mu \frac{\partial u}{\partial \xi} - x_\xi y_\xi \mu \frac{\partial u}{\partial \eta} - x_\xi x_\eta \mu \frac{\partial v}{\partial \xi} + x_\xi^2 \mu \frac{\partial v}{\partial \eta} \right) \right] \\ JS_{vturb} = \sum_{j=1}^2 \frac{\partial}{\partial x_j} (-\rho v' v'_j) = \left\{ \frac{\partial}{\partial \xi} \left( g_{11} \mu_t \frac{\partial v}{\partial \xi} \right) + \frac{\partial}{\partial \xi} \left( g_{12} \mu_t \frac{\partial v}{\partial \eta} \right) + \frac{\partial}{\partial \eta} \left( g_{12} \mu_t \frac{\partial v}{\partial \xi} \right) + \frac{\partial}{\partial \eta} \left( g_{22} \mu_t \frac{\partial v}{\partial \eta} \right) \right\} + \frac{\mu_t}{3} (JS_{vvd}) - \frac{2}{3} \rho \left\{ -\frac{\partial}{\partial \xi} (x_\eta k) + \frac{\partial}{\partial \eta} (x_\xi k) \right\} \\ \mu_t = 0.09 \rho \frac{k^2}{\epsilon} \\ G_k = \frac{4}{3} \left( \frac{u_\xi y_\eta - u_\eta y_\xi}{J} \right)^2 + \frac{4}{3} \left( \frac{-v_\xi x_\eta + v_\eta x_\xi}{J} \right)^2 - \frac{4}{3} \left( \frac{u_\xi y_\eta - u_\eta y_\xi}{J} \right) \left( \frac{-v_\xi x_\eta + v_\eta x_\xi}{J} \right) + 2 \left( \frac{-u_\xi x_\eta + u_\eta x_\xi}{J} \right) \left( \frac{v_\xi y_\eta - v_\eta y_\xi}{J} \right) + \left( \frac{-u_\xi x_\eta + u_\eta x_\xi}{J} \right)^2 + \left( \frac{v_\xi y_\eta - v_\eta y_\xi}{J} \right)^2 \\ - \frac{2}{3} \rho k \left( \frac{u_\xi y_\eta - u_\eta y_\xi - v_\xi x_\eta + v_\eta x_\xi}{J} \right) \\ g_{11} = \left( \frac{x_\eta^2 + y_\eta^2}{J} \right), \quad g_{22} = \left( \frac{x_\xi^2 + y_\xi^2}{J} \right), \quad g_{12} = \left( -\frac{x_\xi x_\eta + y_\xi y_\eta}{J} \right)$$

$$K = \alpha_l K_l + \alpha_v K_v \quad (13)$$

In the VOF model, the total enthalpy in a computational cell can be treated as the mass average of the individual phases as follows:

$$E = \frac{\alpha_v \rho_v E_v + \alpha_l \rho_l E_l}{\alpha_v \rho_v + \alpha_l \rho_l} \quad (14)$$

If the enthalpy is treated as above,  $\chi$ , the average specific heat capacity, has the following form:

$$\chi = \frac{\alpha_l \rho_l C_{v,l} + \alpha_v \rho_v C_{v,v}}{\alpha_l \rho_l + \alpha_v \rho_v} \quad (15)$$

In each computational cell, the evaporation or condensation rates can be determined based on the cell temperature and the mass of the phases. The magnitude of the evaporation process is calculated by Lee [29] as follows:

$$S_v = \beta_1 \alpha_l \rho_l \left| \frac{T - T_{sat}}{T_{sat}} \right| \quad (16)$$

Similarly, for the condensation process:

$$S_l = \beta_2 \alpha_v \rho_v \left| \frac{T - T_{sat}}{T_{sat}} \right| \quad (17)$$

where  $\beta_1$  and  $\beta_2$  are the mass transfer time relaxation parameters which are defined as:

$$\beta_1 = \frac{6}{D_{Sm}} \frac{\sqrt{M}}{\sqrt{2\pi R T_{sat}}} \frac{\rho_v h_{lv}}{\rho_l - \rho_v} \quad (18)$$

$$\beta_2 = \frac{6}{D_{Sm}} \frac{\sqrt{M}}{\sqrt{2\pi R T_{sat}}} \frac{\rho_l h_{lv}}{\rho_l - \rho_v} \quad (19)$$

where  $D_{Sm}$  and  $h_{lv}$  are mean Sauter diameter and latent heat, respectively [30]. In order to numerically maintain the interfacial temperature within  $T_{sat} \pm 1$  K,  $\beta_1$  and  $\beta_2$  need to be fine-tuned. Large values of these parameters induce a numerical oscillation, whereas too small values cause the interfacial temperature to substantially deviate from  $T_{sat}$  [13].

The heat transfer sources corresponded to the evaporation or condensation processes are determined by multiplying the calculated mass transfer with the latent heat, i.e., for the evaporation process:

$$S_E = -S_v h_{lv} \quad (20)$$

And for the condensation process:

$$S_E = S_l h_{lv} \quad (21)$$

The fluid velocity and feed water mass flow rate in  $y$ -direction (or  $\eta$ -direction) are defined at the inlet boundary condition. At the inlet, the fluid velocity in  $x$ -direction ( $\xi$ -direction) and the fluid temperature are equal to zero and the saturation temperature respectively. Therefore:

$$u = 0, \quad v = v_{in}, \quad \alpha_l = 1, \quad T = T_{sat}, \quad k = \frac{3}{2} (v_{in} l)^2, \\ \epsilon = (0.09)^{0.75} k^3 / l^{-1} \quad (22)$$

At the outlet, it is assumed that the fluid has reached to a terminal velocity. Furthermore, the fluid temperature is equal to the saturation temperature. It should be mentioned, changes in

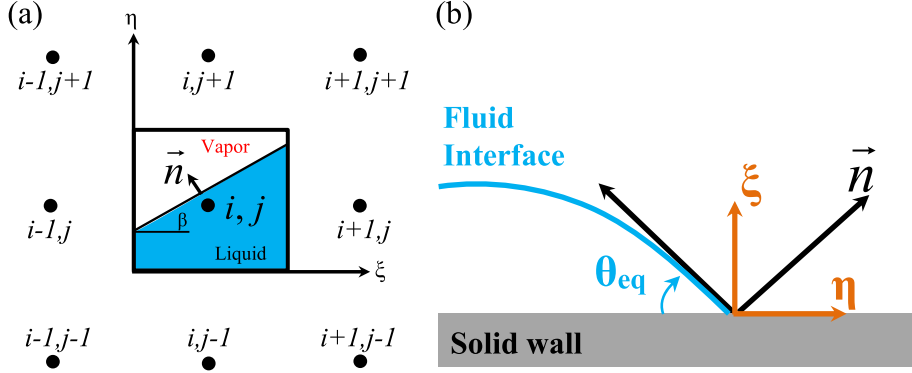


Fig. 2. (a) A schematic of a typical computational cell. (b) Fluid interface near a rigid boundary.

saturation temperature due to the pressure drop are not taken into account in this study. Therefore:

$$u = 0, \frac{\partial v}{\partial y} = 0, T = T_{sat} \quad (23)$$

The boundary conditions at the tube wall are:

$$u = 0, v = 0, T = T_w \quad (24)$$

A symmetry condition is assumed at the right and the left of computational domain as follows:

$$u = 0, \frac{\partial v}{\partial y} = 0, \frac{\partial T}{\partial y} = 0 \quad (25)$$

The heat transfer coefficient at the tube wall is calculated by:

$$h = \frac{-k \frac{\partial T}{\partial n}}{T_w - T_{sat}} = \frac{-k_l}{T_w - T_{sat}} \cdot \frac{1}{\sqrt{g_{22}}} \left( g_{11} \frac{\partial T}{\partial \xi} + g_{22} \frac{\partial T}{\partial \eta} \right) \quad (26)$$

### 3. Numerical validation and grid independency study

The present in-house computational fluid dynamics solver has been verified in our prior publications [16,17,31]. Another comparison study, specifically suitable for the current problem, has

been carried out against the previously published data of Parken et al. [9] to further evaluate the numerical code and non-orthogonal grid discretization scheme of the problem. Their experimental setup was similar to the present model. As observed in Fig. 3, the numerical results and experimental data are fairly in a good agreement with a maximum deviation of 17%.

To clarify the effect of mesh refinement on the numerical solution, three meshes are used in the numerical analysis:  $500 \times 40$ ,  $450 \times 35$  and  $400 \times 30$ . As shown in Fig. 4, increasing the grid numbers does not significantly change the surface Nusselt number. For the  $\Delta T = 4.75^\circ\text{C}$  and  $\dot{m}_f = 0.005 \text{ kg/s}$ ,  $450 \times 35$  grids seem to be optimum in accuracy and run-time. A similar type of grid independence study has been carried out for the other flow and thermal conditions and optimum meshes are chosen (not reported here).

### 4. Solution procedure

The governing equations with appropriate boundary conditions are solved by employing the SIMPLE algorithm [32], a finite-volume method, in a non-orthogonal curvilinear coordinate framework. The Poisson equations are solved for  $(x,y)$  to find grid points [33] and are distributed in a non-uniform manner with higher concentration of grids close to the curvy walls and normal to all walls, as shown in Fig. 1. In this work, a fully implicit scheme is used for the temporal terms and the HYBRID differencing [34] is applied for

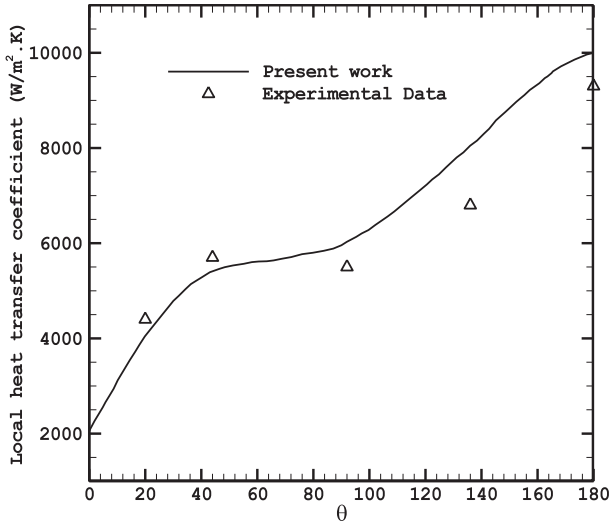


Fig. 3. Validation of numerical code with experimental data Parken et al. [9].

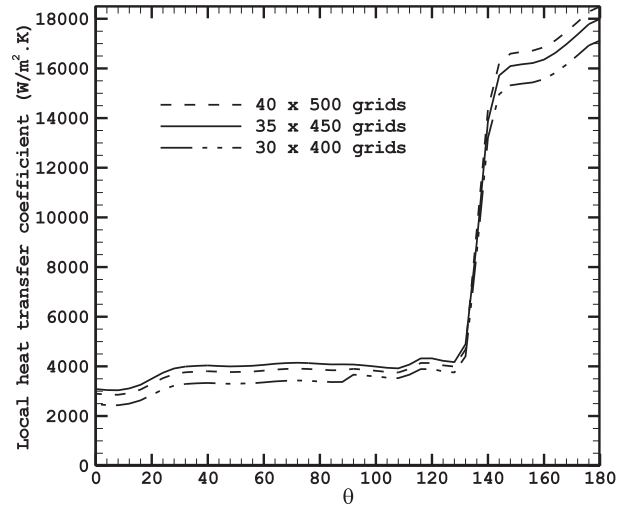
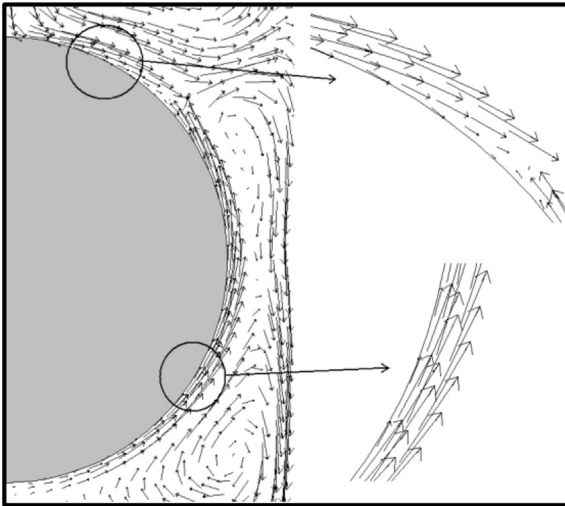


Fig. 4. Numerical results of local heat transfer coefficient around the tube wall at  $\Delta T = 4.75^\circ\text{C}$  and  $\dot{m} = 0.005 \text{ kg/s}$ .



**Fig. 5.** The velocity vectors at  $\Delta T = 9.5 \text{ }^{\circ}\text{C}$  and  $\dot{m}_f = 0.001 \text{ kg/s}$ .

the approximation of the convective terms in a full-staggered grid. In addition, the TDMA (tri-diagonal matrix algorithm) scheme is used to solve the discrete algebraic equations. The governing equations are solved by a SOR (successive over relaxation) method. An under-relaxation technique is employed for a better convergence.

One convergence criteria is a mass flux residual less than  $10^{-7}$  for each control volume. Another criteria is  $(|\phi^{i+1} - \phi^i|)/|\phi^{i+1}| \leq 10^{-8}$ , where  $\phi$  represents any dependent variable, namely  $u$ ,  $v$  and  $T$ , and  $i$  is the number of iteration.

## 5. Results and discussions

A schematic of the geometry along with computational grids is presented in Fig. 1. In this work, only one part of the original geometry (rectangle of ABCD) is numerically solved to reduce the computational time owing to the symmetry conditions. Six tubes with a diameter of 19 mm are investigated. The overall dimensions of the computational domain are 12 mm in x-direction and 300 mm in y-direction. The simulations are conducted for the following

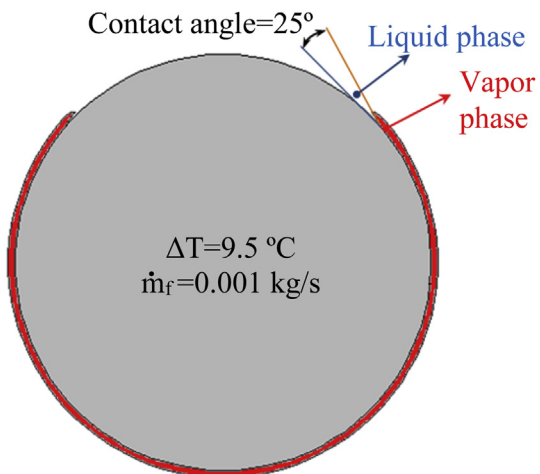


**Fig. 6.** The vapor volume fraction contour corresponding to 0.999 at  $\Delta T = 9.5 \text{ }^{\circ}\text{C}$  and  $\dot{m}_f = 0.001 \text{ kg/s}$ .

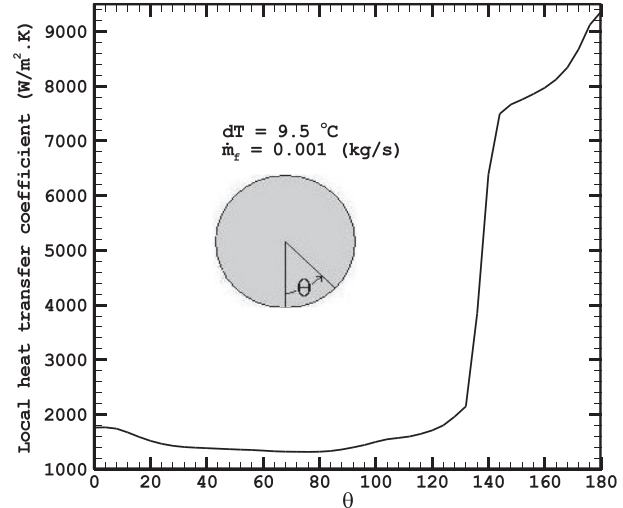


**Fig. 7.** The local heat transfer coefficient at the tube surface at  $\Delta T = 9.5 \text{ }^{\circ}\text{C}$  and  $\dot{m}_f = 0.001 \text{ kg/s}$ .

parameters:  $T_{\text{sat}} = 321.65 \text{ K}$ ,  $\rho_l = 988.7 \text{ kg/m}^3$ ,  $\rho_v = 0.077 \text{ kg/m}^3$ ,  $C_{v,l} = 4327 \text{ J/Kg-K}$ ,  $C_{v,v} = 1465 \text{ J/Kg-K}$ ,  $\mu_l = 560 \text{ } \mu\text{Pa-s}$ ,  $\mu_v = 10.57 \text{ } \mu\text{Pa-s}$ . The saturation temperature inside the evaporator is fixed at  $T_{\text{sat}}$  and the effect of pressure drop on the saturation temperature is not considered. The results are presented for a final time of 10 s. However, a quasi-steady solution is achieved after 7 s in most cases. Numerical calculations are carried out for different values of the inlet feed water mass flow rates ( $\dot{m}_f$ ) and the tube surface superheats ( $\Delta T = T_{\text{tube}} - T_{\text{sat}}$ ).

The velocity vectors at  $\Delta T = 9.5 \text{ }^{\circ}\text{C}$  and  $\dot{m}_f = 0.001 \text{ kg/s}$  are shown in Fig. 5. As it can be seen, at the upper side of the tube, the direction of the fluid is downstream indicating the majority of the fluid is the liquid water flowing downward with a gravitational force. At the lower side of the tube, the fluid direction around the tube is upward implying the major portion of the fluid is the water vapor inclining to flow upward. In order to more clarify the main phenomenological aspects of the problem, the vapor volume

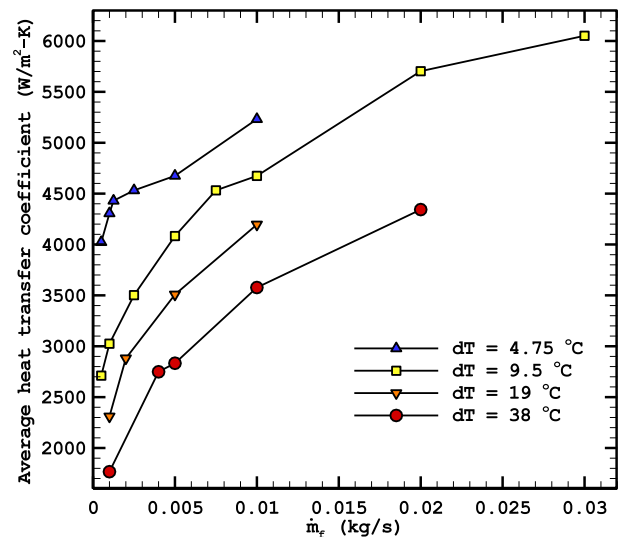


**Fig. 8.** The average heat transfer coefficient versus the inlet mass flow rate at different superheats.

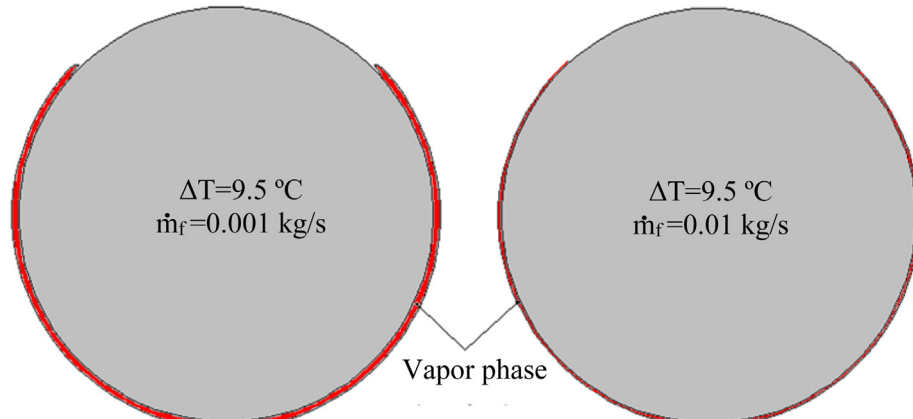


**Fig. 9.** The vapor volume fraction contours corresponding to 0.99 at two different inlet mass flow rates ( $0.001 \text{ kg/s}$  and  $0.01 \text{ kg/s}$ ) for a fixed  $\Delta T = 9.5 \text{ }^{\circ}\text{C}$ .

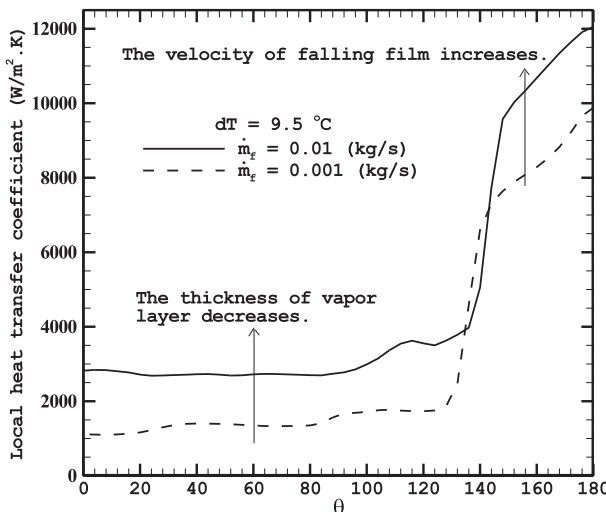


**Fig. 10.** The local heat transfer coefficient at the tube surface at two different inlet mass flow rates ( $0.001 \text{ kg/s}$  and  $0.01 \text{ kg/s}$ ) for a fixed  $\Delta T = 9.5 \text{ }^{\circ}\text{C}$ .

fraction contour of 0.999 for the same conditions of  $\Delta T = 9.5 \text{ }^{\circ}\text{C}$  and  $\dot{m}_f = 0.001 \text{ kg/s}$  is drawn in Fig. 6. As shown, this figure again emphasizes the major portion of the fluid at the lower part of the tube is the water vapor. It can be also found that the liquid water is dominant at the top section of the tube.

The local heat transfer coefficient at the tube surface is depicted in Fig. 7 at  $\Delta T = 9.5 \text{ }^{\circ}\text{C}$  and  $\dot{m}_f = 0.001 \text{ kg/s}$ . As mentioned earlier, the majority of the fluid is the water liquid at the upper side of the tube. This indicates the local heat transfer coefficient is relatively higher compare to the lower side due to a higher thermal conductivity of the liquid water compared to that of the water vapor. In fact, the water vapor presented in the lower side acts as a thermal resistant layer reducing the local heat transfer coefficient.

The effect of the inlet feed water mass flow rate at different tube surface superheats on the average heat transfer coefficient is presented in Fig. 8. At a constant superheat, the results indicate the average heat transfer coefficient enhances as the inlet mass flow rate increases. For instance, at  $\Delta T = 9.5 \text{ }^{\circ}\text{C}$ , the heat transfer coefficient increases by 55% if the inlet mass flow rate varies from  $0.001 \text{ kg/s}$  to  $0.01 \text{ kg/s}$ . To better understand this enhancement in the average heat transfer coefficient, the vapor volume fraction contours corresponding to 0.99 at two different inlet mass flow

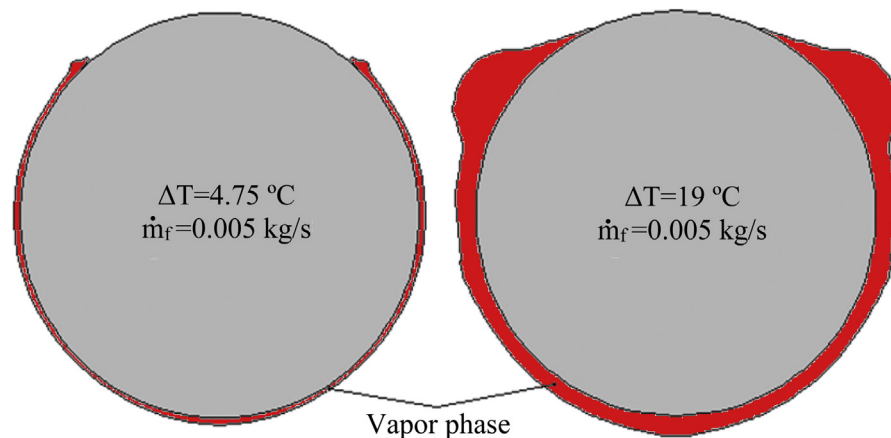


**Fig. 11.** The vapor volume fraction contours corresponding to 0.99 at two different superheats ( $\Delta T = 4.75 \text{ }^{\circ}\text{C}$  and  $\Delta T = 19 \text{ }^{\circ}\text{C}$ ) for a fixed  $\dot{m}_f = 0.005 \text{ kg/s}$ .

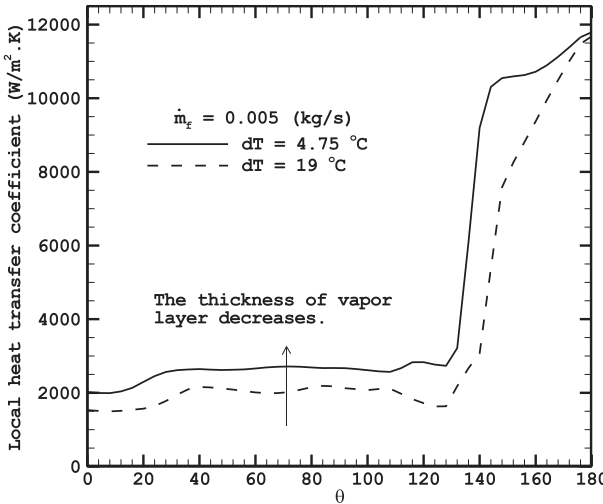


**Fig. 12.** The local heat transfer coefficient at the tube surface at two different superheats ( $\Delta T = 4.75 \text{ } ^\circ\text{C}$  and  $\Delta T = 19 \text{ } ^\circ\text{C}$ ) for a fixed  $\dot{m}_f = 0.005 \text{ kg/s}$ .

rates for a fixed  $\Delta T = 9.5 \text{ } ^\circ\text{C}$  are depicted in Fig. 9. As it can be seen, the thermal boundary layer thickness reduces as the inlet mass flow rate increases at a constant superheat resulting in an enhancement in the average heat transfer coefficient. It is worthwhile to show the local heat transfer coefficient at the tube surface for these two cases (cf. Fig. 10). As expected, the local heat transfer coefficient increases at higher inlet mass flow rates if the superheat is kept constant. This enhancement in the local heat transfer has two different reasons at the upper and lower sides of the tube. At the upper side of the tube, the fluid velocity and the convective heat transfer effects are magnified by an increase in the inlet mass flow rate. At the lower part of the tube, the enhancement in the local heat transfer coefficient is due to a decrease in the thermal boundary layer thickness.

Fig. 8 also shows that the average heat transfer coefficient decreases at higher superheats if the inlet mass flow rate is kept

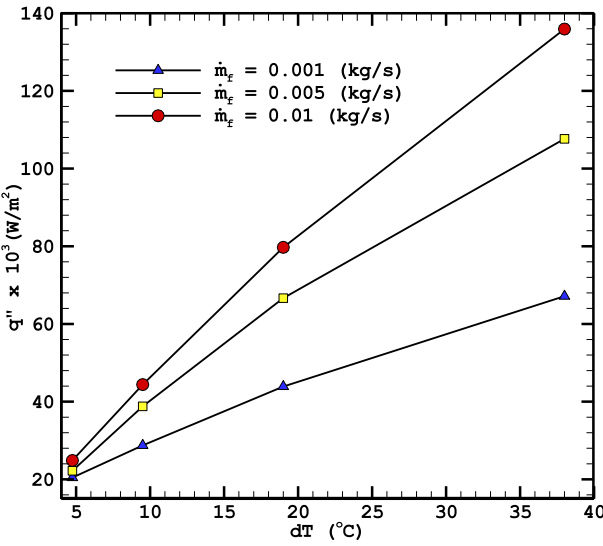


**Fig. 13.** Variations of the local heat flux with the superheat at different inlet mass flow rates.

constant. For example, the heat transfer coefficient decreases by 12% if the superheat varies from  $\Delta T = 4.75 \text{ } ^\circ\text{C}$  to  $\Delta T = 9.5 \text{ } ^\circ\text{C}$  for a fixed  $\dot{m}_f = 0.005 \text{ kg/s}$ . To better understand the effect of the superheat on the heat transfer coefficient, the vapor volume fraction contours corresponding to 0.99 at two different superheats for a fixed  $\dot{m}_f = 0.005 \text{ kg/s}$  are depicted in Fig. 11. As this figure clearly shows, the thermal boundary layer thickness grows as the surface superheat increases at a constant inlet mass flow rate resulting in a reduction in the average heat transfer coefficient at the tube surface. The local heat transfer coefficient at the tube surface for these two cases is shown in Fig. 12. When the surface superheat increases from  $4.75 \text{ } ^\circ\text{C}$  to  $19 \text{ } ^\circ\text{C}$  at a constant inlet mass flow rate, the high heat transfer coefficient region at the top side of the tube is dramatically shrunk. This is largely due to the stretching of water vapor layer to the top side of the tube. Fig. 12 also indicates the local heat transfer coefficient decreases when the superheat increases at a constant inlet mass flow rate.

The variations of the local heat flux ( $q'' = h\Delta T$ ) as a function of the surface superheat at different inlet mass flow rates are shown in Fig. 13. As the degree of the superheat increases at a constant inlet mass flow rate, the heat transfer coefficient tends to decrease the heat flux, whereas the surface superheat works to increase the heat flux. As this figure implies, the effect of superheat is more significant than the decreasing effect of heat transfer coefficient on the heat flux resulting in an increase in the local heat flux.

The interconnected effects of the inlet mass flow rate and the superheat on the average heat transfer coefficients are depicted in Fig. 14. This is an important condition in multi effect desalination with thermal vapor compression (MED-TVC) units in which a constant ratio of  $\Delta T$  to  $\dot{m}_f$  is specified during the design phase of each individual MED unit [35]. The diagram can be considered as practical thermal performance curves of falling film evaporators utilized in the MED units both in the design stage and the operation phase of these units. As shown, the diagram has two distinct trends for a fixed  $\Delta T/\dot{m}_f$ . In the region I, as the inlet mass flow rate and consequently the superheat increases, the average heat transfer coefficient decreases. As it has been already mentioned, the superheat and the inlet mass flow rate have opposite effects on the heat transfer coefficient. This means the effect of the superheat on the average heat transfer coefficient is more dominant than the

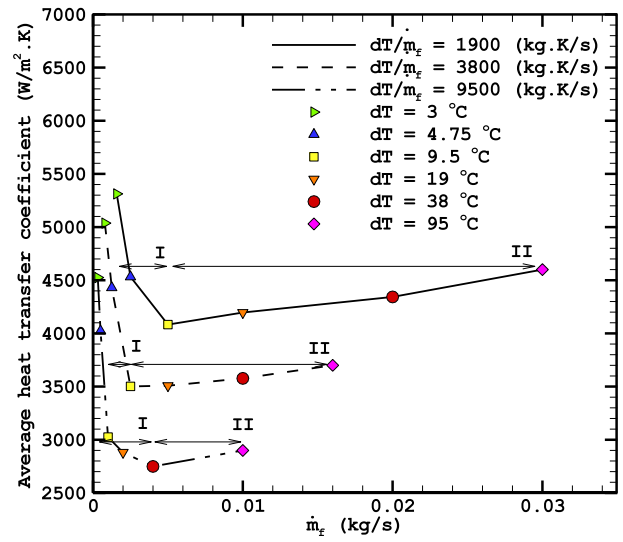


**Fig. 14.** Variations of the average heat transfer coefficient with the inlet mass flow rate at different values of  $\Delta T/\dot{m}_f$  (performance curves).

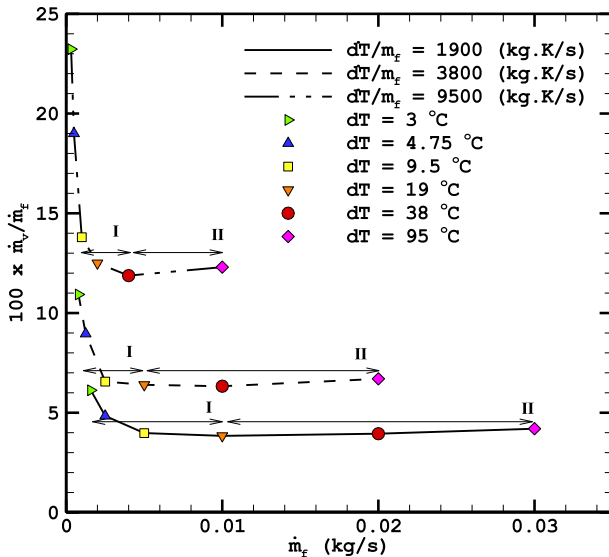


**Fig. 15.** Variations of the net water vapor production percentage versus the inlet mass flow rate at different values of  $\Delta T/m_f$ .

other effect in region I. In contrast the increasing effect of the inlet mass flow rate on the average heat transfer coefficient overcomes the decreasing effect of the superheat in region II. The graph also points out that the transition wall superheat separating region I and II increases as the values of  $\Delta T/m_f$  increases. The presented performance curves provide more insights into the operation conditions of MED plants during their design phase.

The percentage of net water vapor production,  $\dot{m}_v/\dot{m}_f^*$ , as function of the inlet mass flow rate is plotted in Fig. 15 at different values of  $\Delta T/m_f$ . As it can be noticed, at a constant value of  $\Delta T/m_f$ , the vapor quality decreases when the inlet mass flow rate increases in region I. For instance, the vapor quality decreases by 49% if the inlet mass flow rate varies from 0.000316 (kg/s) to 0.004 (kg/s) at  $\Delta T/m_f = 9500$ . The decreeing effect of the inlet mass flow rate at a constant value of  $\Delta T/m_f$  on the vapor quality is almost vanishes in region II in which a higher superheat is available. This graph can be also helpful in the design phase of MED plants.

Here, the experimental results of two operational MED-TVC units (Fan Niroo Company [36]), one having two effects and another four effects, are selected to relatively compare the operational test data of these units with the obtained thermal performance curves (cf. Fig. 14). In MED units, each effect refers to a tube bundle shield in which the vapor inside the tubes comes from the

evaporated falling liquid water of the previous effect. The selected MED units have a total distilled product of 64 ton/hour. Fig. 16 shows a picture of these MED-TVC units. The experimental data extracted from the HMI (human machine indicator) of these units are shown in Table 2.

The average superheat between the tube temperature and the effect temperature is 4.8 °C and 10.5 °C for the MED units with four and two effects respectively. The ratio of  $\Delta T$  to  $\dot{m}_f$  in both experimental units is approximately 3600.

Since the total distilled product is the same in these two units, it can be concluded:

$$\left. \frac{\bar{h}_2 \text{ effects}}{\bar{h}_4 \text{ effects}} \right|_{\text{Experimental Data}} = \frac{(\Delta T)_4 \text{ effects}}{(\Delta T)_2 \text{ effects}} = 0.9 \quad (27)$$

This means, at a constant value of  $\Delta T/m_f$ , the average heat transfer coefficient (the thermal performance) decreases when the number of effects in the MED desalination units is reduced. It should be noted that, at a constant value of  $\Delta T/m_f$ , a decrease in the number of MED effects is equal to an increase in the mass flow rate of the feed water. As the performance curves of the MED units demonstrated, the thermal performance may decrease or increase by an increase in the feed water mass flow rate at a constant value of  $\Delta T/m_f$  (Region I or II in Fig. 14). To understand the operating region of a specific MED desalination unit, one should consider the values of  $\Delta T/m_f$  and the tube surface superheat. Regarding the given data in Table 2 and calculated data, both mentioned experimental units would work in Region I of the performance curve. At the next step, the numerical code is executed according to the conditions of the two experimental units. For the case of  $\Delta T/m_f = 3600$  and  $\Delta T = 4.8$  °C (corresponding to the MED unit with four effects), the numerical simulation gives 4410 (W/m<sup>2</sup>-K) as the average heat transfer coefficient. For the case of  $\Delta T/m_f = 3600$  and  $\Delta T = 10.5$  °C (corresponding to the MED unit with two effects), the average heat transfer coefficient is 3654 (W/m<sup>2</sup>-K). Therefore

$$\left. \frac{\bar{h}_2 \text{ effects}}{\bar{h}_4 \text{ effects}} \right|_{\text{Numerical Data}} = 0.83 \quad (28)$$

As observed, similar to the experimental data, the obtained performance curve shows the average heat transfer coefficient decreases by a decrease in the number of effects in the MED desalination units (or an increase in the feed water mass flow rate) at a constant value of  $\Delta T/m_f$ . It can be seen that there is a good agreement between the experimental data extracted from these MED-TVC units and the corresponding numerical data with a deviation of about 7.7%.

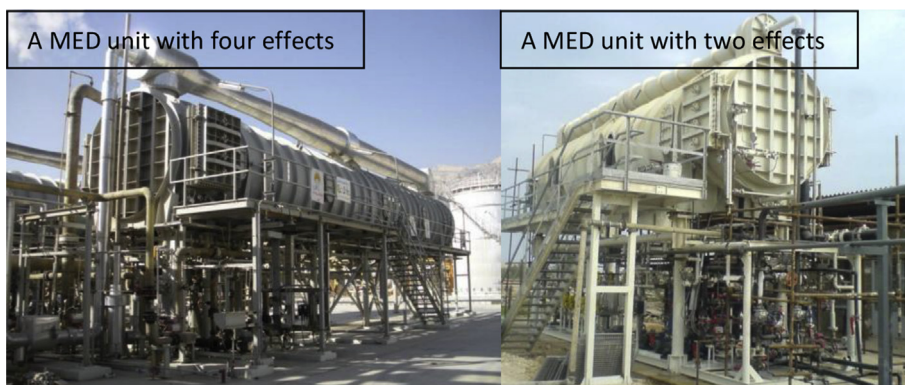


**Fig. 16.** Pictures of experimental units with four and two effects.

**Table 2**

The operational data of two experimental MED-TVC units.

Number of effects	4	2
Total distilled product, ton/hr	64	64
Total feed water mass flow rate, ton/hr	216	216
Feed water mass flow rate per effect, ton/hr	54	108
Steam consumption, ton/hr	9.6	21
Entertainment ratio	0.875	0.7
Feed water temperature, °C	45	45
Discharge temperature, °C	65	70.7
First effect temperature, °C	59.8	59.8
Second effect temperature, °C	55.1	49.7
Third effect temperature, °C	50.5	—
Forth effect temperature, °C	45.7	—
Condenser temperature, °C	45.2	49.2
Specific heat transfer surface area	216	108

## 6. Conclusion

Two-phase flow simulation of falling film evaporation phenomenon on a horizontal tube bundle had been studied using the VOF (volume of fluid) multiphase model based on a PLIC (piecewise linear interface construction) method in a curvilinear coordinate. Simultaneous interphase heat and mass transfers were also taken into account. The governing equations including continuity, energy and RANS (Reynolds averaged Navier–Stokes) equations with the  $k-\epsilon$  turbulence model were solved by a finite volume method code based on the SIMPLE algorithm in a non-orthogonal discretization grid system.

Results showed the average heat transfer coefficient increases at higher inlet mass flow rate if the tube surface superheat is kept constant. It was also found that an increase in the superheat results in a decrease in the average heat transfer coefficient for a fixed inlet mass flow rate. In addition, practical thermal performance curves of the falling film evaporators utilized in the MED units are presented. The performance curves demonstrated, at a constant value of  $\Delta T/m_f$  which is a fixed designed parameter of the MED-TVC units, the thermal performance of the MED units first decreases and then increases as the inlet mass flow rate increases. The presented results provide basic guidelines for the design stage as well as the operation phase of the MED units.

## References

- [1] Thome JR. Falling film evaporation: state-of-the-art review of recent work. *J Enhanc Heat Transf* 1999;6:263–77.
- [2] Ribatski G, Jacobi AM. Falling-film evaporation on horizontal tubes—a critical review. *Int J Refrig* 2005;28:635–53.
- [3] Thome JR. Chapter 14: falling film evaporation. *Eng. Datab. III.* 2006.
- [4] Li W, Wu X-Y, Luo Z, Yao S, Xu J-L. Heat transfer characteristics of falling film evaporation on horizontal tube arrays. *Int J Heat Mass Transf* 2011;54:1986–93.
- [5] Åslad A, Berntsson T. Surface evaporation of turbulent falling films. *Int J Heat Mass Transf* 1991;34:835–41.
- [6] Parken WH. Heat transfer to thin films on horizontal tubes. 1975.
- [7] Fujita Y, Tsutsui M. Experimental investigation of falling film evaporation on horizontal tubes. *Heat Transf Jpn Res* 1998;27:609–18.
- [8] Chyu M-C, Bergles AE. An analytical and experimental study of falling-film evaporation on a horizontal tube. *J Heat Transf* 1987;109:983.
- [9] Parken WH, Fletcher LS, Sernas V, Han JC. Heat transfer through falling film evaporation and boiling on horizontal tubes. *J Heat Transf* 1990;112:744.
- [10] Yang L, Shen S. Experimental study of falling film evaporation heat transfer outside horizontal tubes. *Desalination* 2008;220:654–60.
- [11] Habert M, Thome JR. Falling-film evaporation on tube bundle with plain and enhanced tubes—part I: experimental results. *Exp Heat Transf* 2010;23:259–80.
- [12] Habert M, Thome JR. Falling-film evaporation on tube bundle with plain and enhanced tubes—part II: new prediction methods. *Exp Heat Transf* 2010;23:281–97.
- [13] Yang Z, Peng XF, Ye P. Numerical and experimental investigation of two phase flow during boiling in a coiled tube. *Int J Heat Mass Transf* 2008;51:1003–16.
- [14] Son G, Dhir VK. Numerical simulation of saturated film boiling on a horizontal surface. *J Heat Transf* 1997;119:525.
- [15] Yuan MH, Yang YH, Li TS, Hu ZH. Numerical simulation of film boiling on a sphere with a volume of fluid interface tracking method. *Int J Heat Mass Transf* 2008;51:1646–57.
- [16] Shokoumand H, Bigham S. Slip-flow and heat transfer of gaseous flows in the entrance of a wavy microchannel. *Int Commun Heat Mass Transf* 2010;37:695–702.
- [17] Shokoumand H, Bigham S, Nasr Isfahani R. Effects of Knudsen number and geometry on gaseous flow and heat transfer in a constricted microchannel. *Heat Mass Transf* 2010;47:119–30.
- [18] Ashjaee M, Bigham S, Yazdani S. A numerical study on natural convention heat transfer from a horizontal isothermal cylinder located underneath an adiabatic ceiling. *Heat Transf Eng* 2013;35:953–62.
- [19] Ashjaee M, Yazdani S, Bigham S, Yousefi T. Experimental and numerical investigation on free convection from a horizontal cylinder located above an adiabatic surface. *Heat Transf Eng* 2011;33:213–24.
- [20] Hassan YA, Barsamian HR. New-wall modeling for complex flows using the large eddy simulation technique in curvilinear coordinates. *Int J Heat Mass Transf* 2001;44:4009–26.
- [21] Hoffmann KA, Chiang ST. Computational fluid dynamics. *Engineering Education System*; 2000.
- [22] Anderson JD. Computational fluid dynamics the basics with applications. *McGraw-Hill Education*; 1995.
- [23] Zaleski S. Interface tracking—VOF. In: Lecture given at course: industrial two-phase flow CFD. Von Karman Institute for Fluid Dynamics; 2005.
- [24] Li J. Piecewise linear interface calculation. *Comptes Rendus de l Academie des Sciences Serie II. Fascicule B-Mecanique*. 1995.
- [25] Tennekes H, Lumley JL. *A first course in turbulence*. The MIT Press; 1972.
- [26] Parker BJ, Youngs DL. Two and three dimensional Eulerian simulation of fluid flow with material interfaces. Technical report. 1992.
- [27] Scardovelli R, Zaleski S. Direct numerical simulation of free-surface and interfacial flow. *Annu Rev Fluid Mech* 1999;31:567–603.
- [28] Brackbill J, Kothe D, Zemach C. A continuum method for modeling surface tension. *J Comput Phys* 1992;100:335–54.
- [29] Lee WH. A pressure iteration scheme for two-phase flow modeling, multiphase transport fundamentals, reactor safety, applications. Washington, DC: Hemisphere Publishing; 1980.
- [30] Crowe C, Sommerfeld M, Tsuji Y. *Multiphase flows with droplets and particles*. CRC Press; 1998.
- [31] Bigham S, Shokoumand H, Isfahani RN, Yazdani S. Fluid flow and heat transfer simulation in a constricted microchannel: effects of rarefaction, geometry, and viscous dissipation. *Numer Heat Transf Part A Appl* 2011;59:209–30.
- [32] Patankar S, Spalding D. A calculation procedure for heat, mass and momentum transfer in three-dimensional parabolic flows. *Int J Heat Mass Transf* 1972;15:1787–806.
- [33] Hoffman KA. Computational fluid dynamics for engineers. Austin: *Engineering Education System*; 1989.
- [34] Spalding DB. A novel finite difference formulation for differential expressions involving both first and second derivatives. *Int J Numer Methods Eng* 1972;4:551–9.
- [35] Kouhikamali R. Thermodynamic analysis of feed water pre-heaters in multiple effect distillation systems. *Appl Therm Eng* 2013;50:1157–63.
- [36] Fan Niroo Company. 1992. [www.fanniroo.com](http://www.fanniroo.com).